Sensors & Actuators: A. Physical 408 (2026) 117938

Contents lists available at ScienceDirect

Sensors and Actuators: A. Physical

journal homepage: www.journals.elsevier.com/sensors-and-actuators-a-physical

Tip position estimation of a 3-DOF soft mechanism using artificial muscles with optical fibers

Rikimaru Okada, Shuichi Wakimoto *, Yuichiro Toda, Shun Miura, Daisuke Yamaguchi, Takefumi Kanda

Graduate School of Environment, Life, Natural Science and Technology, Okayama University, 3-1-1 Tsushima-naka, Kita-ku, Okayama 700-8530, Japan

ARTICLE INFO

Keywords:
Pneumatic artificial muscle
Smart artificial muscle
Soft mechanism
State estimation
Long short-term memory

ABSTRACT

McKibben-type pneumatic artificial muscles (PAMs) are lightweight and flexible soft actuators with a high power-to-weight ratio, and have been widely applied to rehabilitation devices, power-assist systems, and soft robotic mechanisms. By integrating sensing functions into PAMs, their usability and controllability can be enhanced, enabling the development of more practical and advanced soft mechanisms. We previously proposed a smart artificial muscle (SAM) by integrating an optical fiber into the braided sleeve of a McKibben-type PAM, which enables displacement estimation by measuring optical bending loss. The SAM is compatible with conventional PAM fabrication processes; however, the sensor output exhibits strong nonlinearity and time dependency. In this study, an LSTM-based state estimation framework is extended from a single SAM to a three-degree-of-freedom soft mechanism composed of multiple SAMs, where strong nonlinear coupling and mutual interference arise among actuators. In the proposed framework, the LSTM model jointly processes time-series data of multi-channel optical sensor outputs and applied pressures of the three SAMs, along with past estimated states as inputs. This structure enables the model to capture nonlinear coupling, hysteresis, and time-dependent behavior, allowing estimation of the tip position of the soft mechanism. Experimental results demonstrate that the proposed method accurately captures complex nonlinear dynamics and mutual mechanical interference among multiple SAMs, achieving accurate tip position estimation. These results indicate that SAMs with integrated sensing and actuation capabilities, combined with machine-learning-based estimation, provide an effective approach for state estimation of multi-DOF soft robotic mechanisms.

1. Introduction

McKibben-type pneumatic artificial muscles (PAMs) are soft actuators characterized by flexibility, lightweight, and a high power-to-weight ratio [1–6]. Owing to their simple structure, PAMs, including McKibben-type and bending-type, have been widely applied in rehabilitation devices, power-assist systems, robotic manipulators and grippers [7–12]. However, the nonlinear mechanical properties and viscoelasticity of elastomer materials, as well as frictional forces between fibers, result in complex output characteristics. These factors make accurate estimation of displacement and output force a significant challenge.

Conventional rigid robotic mechanisms, such as articulated robotic arms, are typically driven by electromagnetic motors equipped with encoders, which play a crucial role in achieving high controllability. The integration of motors and encoders is a well-established engineering practice. By analogy, artificial muscles equipped with integrated sensing functions would significantly enhance the controllability and practicality of soft mechanisms, while maintaining their simple configuration and fabrication process. Such sensor-integrated artificial muscles can eliminate the need for external sensing systems. Accordingly, various studies have investigated soft actuators and soft robots with embedded or integrated sensors [13–20], and state estimation and data-driven modeling by machine learning [21–25].

The authors previously developed a Smart Artificial Muscle (SAM) by integrating an optical fiber into the braided sleeve of a McKibben-type PAM. By measuring the optical loss induced in the optical fiber, the contraction of the muscle was estimated [26]. Because the sensing signal is optical, it is inherently resistant to electromagnetic noise from the surrounding environment. In addition, this approach offers a manufacturing advantage: optical fibers can be installed in the braiding machine in place of conventional fibers, allowing SAMs to be fabricated

* Corresponding author.
E-mail address: wakimoto@okayama-u.ac.jp (S. Wakimoto).

https://doi.org/10.1016/j.sna.2026.117938
Received 15 January 2026; Received in revised form 16 April 2026; Accepted 30 April 2026
Available online 2 May 2026

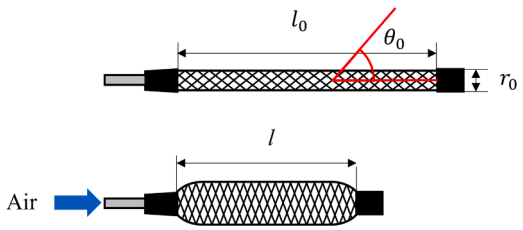

Fig. 1. Configuration of a McKibben-type pneumatic artificial muscle (PAM).

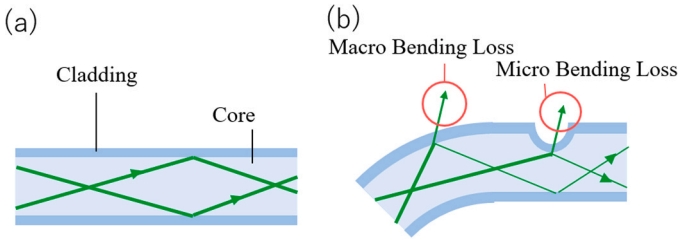

Fig. 2. Propagation of light in an optical fiber: (a) total internal reflection, (b) bending loss.

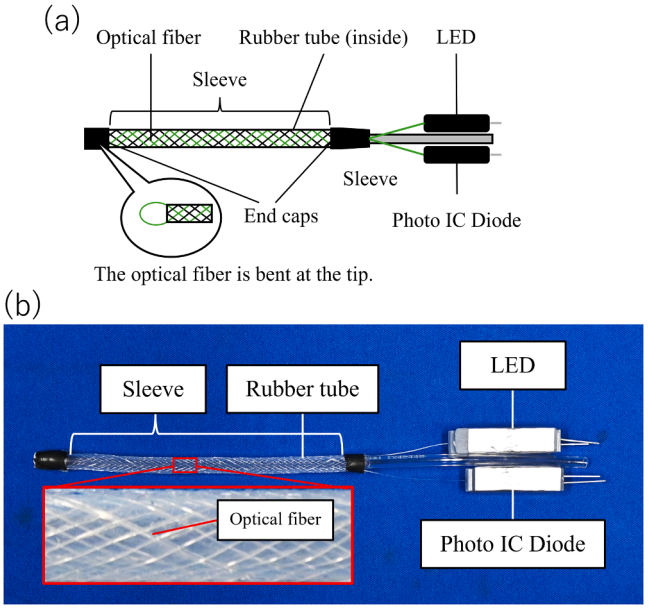

Fig. 3. Optical fiber composite smart artificial muscle (SAM): (a) schematic diagram, (b) photograph.

using the same process as standard PAMs without any other embedding steps.

Experimental results, however, revealed that the optical sensor output shows non-linearity and time dependency, and depends not only on displacement of the muscle but also on internal pressure and external loads. To address these complex sensor characteristics, machine-learning-based estimation was introduced. In particular, a Long Short-Term Memory (LSTM) network was applied to estimate the muscle length using time-series data of applied pressure and optical sensor output. The results demonstrated that machine learning can effectively compensate for the complex and nonlinear sensing characteristics of SAMs [26].

In this study, as an application of SAMs, a three-degree-of-freedom (3-DOF) soft mechanism is developed. The mechanism consists of three SAMs arranged in parallel and enables bending motion. The LSTM network is extended and applied to the proposed soft mechanism. By jointly processing time-series data including optical sensor outputs and applied pneumatic pressures of the three SAMs, the tip position of the mechanism is estimated. This approach addresses the strong non-linearities, temporal dependencies and mutual mechanical interactions inherent in multi-DOF soft mechanism, enabling a high-accuracy and robust state estimation system suitable for practical applications. The results indicate that SAMs integrating sensing and actuation capabilities are effective components for constructing soft robotic systems.

2. Configuration of 3-DOF mechanism

2.1. McKibben-type PAM

The McKibben-type PAM is a lightweight and highly flexible soft actuator composed of an inner elastic tube and an outer braided fiber sleeve. A schematic model of the McKibben-type PAM is shown in Fig. 1. When pressurized, the braided fibers function as a pantograph mechanism, causing the PAM to expand radially and contract axially. The resulting contraction force and displacement are utilized as the driving source for various soft robotic systems.

Focusing on the geometric deformation of the fibers within the sleeve, it is known that the radius of curvature of the helical fibers R varies depending on the muscle length. This relationship can be expressed by Eq. (1), assuming an initial diameter r_0, an initial length l_0, and an initial braid angle θ_0 as constants [27].

$$R = \frac{r_0}{\sin\theta_0 \sqrt{1 - \left(\frac{l}{l_0}\right)^2 \cos^2\theta_0}} \tag{1}$$

2.2. Optical fiber

The structure of the optical fiber is shown in Fig. 2(a). The fiber consists of two layers: a central core and a surrounding cladding. The cladding is designed to have a lower refractive index than the core. When light is incident on the interface between the core and cladding at an angle exceeding the critical angle, it becomes confined within the core and propagates through the fiber by total internal reflection.

However, when the fiber is bent, as illustrated in Fig. 2(b), portions of the incident light fall below the critical angle, causing part of the optical signal to leak out of the fiber. This phenomenon, known as macro-bending loss [28,29], increases as the bending radius decreases, resulting in reduced transmitted light intensity. In addition, when localized pressure is applied to the surface of the optical fiber, small deformations occur, leading to micro-bending loss [30], in which light leaks from the deformed segments.

The total amount of light transmitted through the optical fiber is therefore determined by the combined effects of macro-bending and micro-bending losses.

2.3. Configuration of SAM with optical fiber

As shown in Fig. 3, the SAM incorporates a 0.5-mm-diameter optical fiber as one of its structural elements. The actuator can be fabricated easily using a braiding machine [27]. The actuator section has a total length of 100 mm and a diameter of 5 mm. As illustrated in Fig. 3(a), the rubber tube is covered by several synthetic fibers together with a single optical fiber that is folded back at its tip. A fabricated example is shown in Fig. 3(b).

To realize the sensing functionality, the optical fiber requires a light-emitting device and a photodetector at its two ends in general. These components are used to measure variations in the optical intensity transmitted through the fiber. Both the light source and the photodetector are integrated on the root side of the SAM, which greatly simplifies wiring and component placement when embedding the actuator into robotic mechanisms. For this reason, the optical fiber is folded back

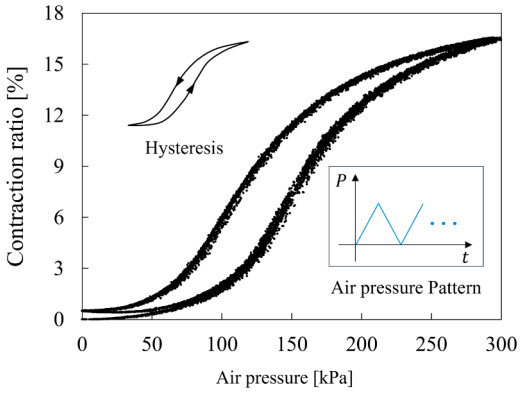

Fig. 4. Relationship between applied pressure and contraction ratio of the SAM.

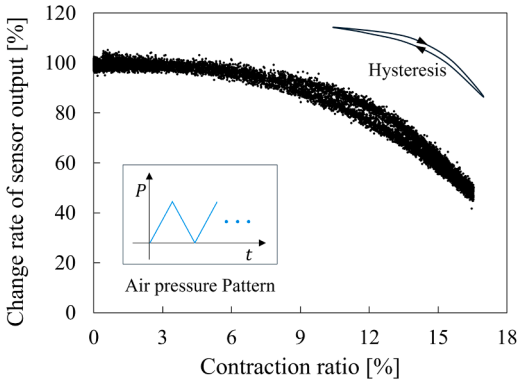

Fig. 5. Relationship between contraction ratio and sensor output of the SAM.

at the tip of the actuator. As the light- emitting and receiving devices, an LED (Cree LED, model: C503B-GAN-CB0F0791) and a photo IC diode (Hamamatsu Photonics, model: S13948–01SB) are used. These electronic components are mounted on a 3D-printed connector and shielded with aluminum tape to suppress external optical noise.

To evaluate the actuation characteristics, the applied pressure was increased from 0 kPa to 300 kPa over 30 s and then decreased back to 0 kPa over the subsequent 30 s. This cycle was repeated five times while measuring the applied pressure, contraction ratio, and sensor output. The relationship between the applied pressure and the contraction ratio is shown in Fig. 4, and the relationship between the contraction ratio and the sensor output is shown in Fig. 5.

From Fig. 4, the maximum contraction ratio of the SAM is approximately 16.5%. Hysteresis is observed, which is a well-known phenomenon inherent to this class of soft actuators. Furthermore, as shown in Fig. 5, the sensor output decreases with increasing contraction ratio due to bending loss in the optical fiber. These results indicate the nonlinear characteristics of the SAM in both actuation and sensing.

2.4. Configuration of 3-DOF soft mechanism

The 3-DOF soft mechanism developed in this study is shown in Fig. 6, and its actuation principle is illustrated in Fig. 7. The mechanism consists of three SAMs —SAM 1, SAM 2, and SAM 3—arranged evenly around the circumference and connected by a common base and end cap. By independently actuating each SAM, the mechanism can achieve arbitrary tip positions within a three-dimensional workspace. A

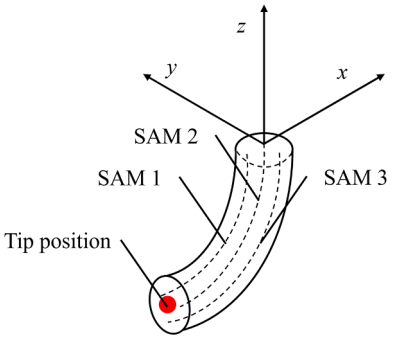

Fig. 7. Geometric configuration of the 3-DOF soft mechanism composed of three circumferentially arranged SAMs.

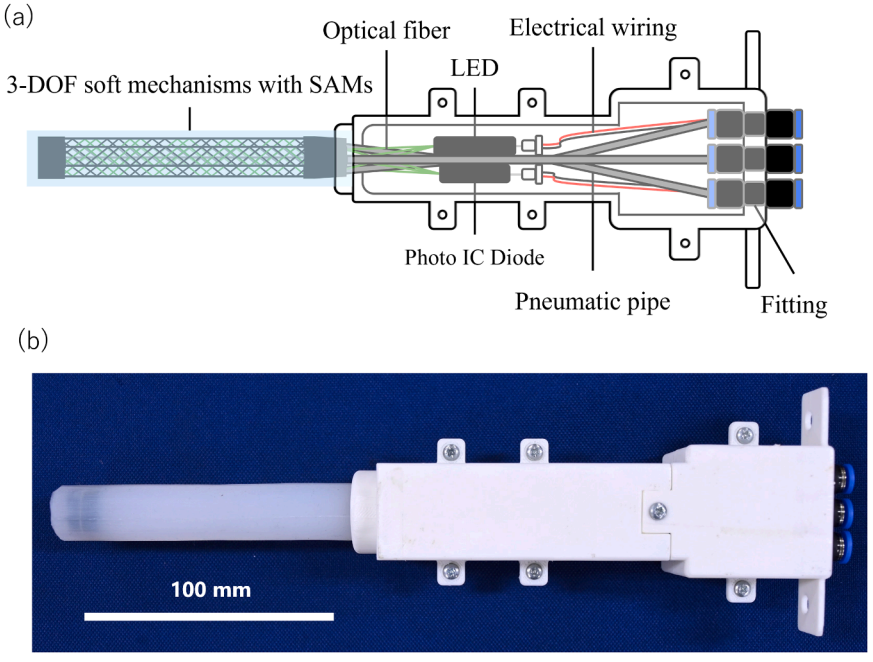

Fig. 6. Structure of the 3-DOF soft mechanism: (a) schematic diagram, (b) photograph.

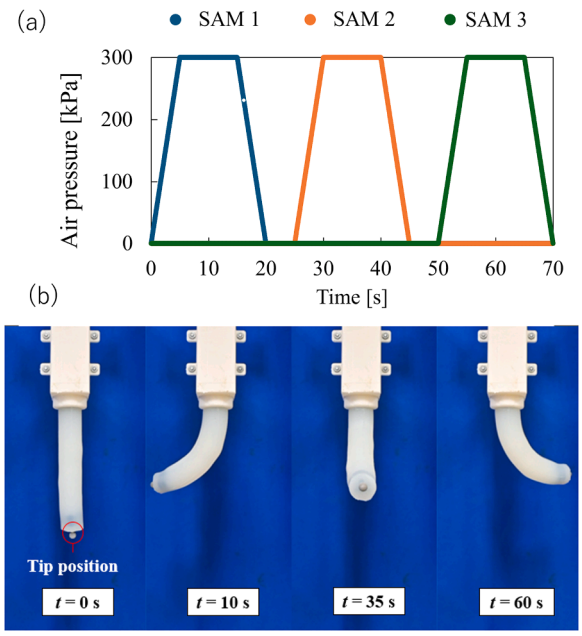

Fig. 8. Fundamental experiment conditions: (a) applied pressure pattern, (b) bending motion of the mechanism.

dedicated housing is fabricated to protect and secure the light-emitting and light-receiving devices integrated into each SAM.

As depicted in the geometric model in Fig. 7, the independent pressurization and resulting contraction of each SAM determine both the bending direction and bending magnitude of the mechanism according to the contraction ratios of the three actuators.

In this study, the geometric coordinate system of the 3-DOF soft mechanism is defined such that the radial plane corresponds to the x-y plane, and the axial direction corresponds to the z axis.

2.5. Fundamental characteristics of 3-DOF soft mechanism

As a fundamental actuation experiment, the pneumatic command inputs shown in Fig. 8(a) were applied to each electro-pneumatic regulator to evaluate the motion of the 3-DOF soft mechanism. Fig. 8 (b) shows the mechanism during actuation, and Fig. 9 illustrates (a) the relationship between the optical fiber sensor outputs of SAM 1, SAM 2, and SAM 3 and the corresponding tip-position coordinates, and (b) the time-series changes in the sensor signals of each muscle.

From Fig. 8, pressurizing a specific SAM causes that actuator to contract, resulting in bending of the entire soft mechanism toward the direction of the contracted SAM. Specifically, when pressure was applied to SAM 1 at $t = 10$ s, the mechanism bent toward the SAM 1 direction, whereas at $t = 35$ s and $t = 60$ s, it bent toward the SAM 2 and SAM 3 directions, respectively. Fig. 9(a) shows that the sensor output corresponding to the bending direction decreases, indicating that the optical fiber sensor reflects the deformation behavior of the soft mechanism. Although this soft mechanism can generate diverse motions by independently actuating each SAM, mechanical coupling among the SAMs introduces complex characteristics into the sensing behavior. First, because each SAM is composed of compliant materials, pronounced nonlinearities and hysteresis exist in the displacement and sensor output. In addition, the sensor output depends not only on the SAM length but also on applied pressure and external loads. This is due to localized high-stress regions that arise from pressurized rubber deformation or external tensile forces, thereby increasing micro-bending loss in the optical fiber [31]. Moreover, when pressure is applied to one SAM, tensile or compressive forces are transmitted to the other SAMs, influencing their sensor outputs as well. Consequently, the sensor outputs cannot be described by a single variable, but instead exhibit interdependent relationships across the three SAMs.

Indeed, Fig. 9(b) illustrates the temporal evolution of each sensor output from $t = 0$–25 s. During this period, pressure was applied only to SAM 1. However, not only the sensor output of SAM 1 but also those of SAM 2 and SAM 3 changed. The sensor signals exhibit temporal- and hysteresis-dependent behavior with complex time-series characteristics. Taken together, the sensing outputs of this soft mechanism are influenced by the SAM lengths, applied pressures, external loads, and inter-SAM mechanical interactions, resulting in strong nonlinearity, hysteresis, and temporal dependency. These factors make the construction of an analytical mathematical model highly challenging.

The maximum applied pressure for each SAM is set to 300 kPa based on safe operation limits, and the maximum curvature was found to be 14 m^{-1}. The maximum payload was evaluated experimentally by gradually increasing the mass attached to the tip in increments of 100 g. It was observed that at 500 g, the motion range became extremely limited. Therefore, the maximum payload is defined as 400 g in this study.

3. Machine learning for tip position estimation

3.1. Machine learning setup

Because the sensor characteristics exhibit nonlinearity, hysteresis, temporal behavior, and mutual interference among SAMs, a powerful recurrent neural network based on Long Short-Term Memory (LSTM) is employed [31]. The LSTM-based model enables accurate estimation even under fluctuating complex sensor outputs [25,26].

Fig. 10 illustrates the overall architecture of the neural network, and Table 1 summarizes the main hyperparameters used for training. The model is a time-series regression model composed of three LSTM layers with a dropout layer for preventing overfitting [32], and a final fully connected output layer. The model input consists of nine channels: the applied pressures to the three SAMs (P_{1t}, P_{2t}, P_{3t}), the three-channel outputs of the optical fiber sensors embedded in each SAM (S_{1t}, S_{2t}, S_{3t}), and the estimated tip position of the mechanism at the previous time step ($\hat{x}_{t-1}$, $\hat{y}_{t-1}$, $\hat{z}_{t-1}$), where t denotes the time step. This model reflects the nonlinear and interactive characteristics of the sensors and incorporates temporal dependencies by feeding back the previous output as input [33].

To further capture the time- and history-dependent behavior, a look-back window of 30 consecutive time steps was employed. The model outputs the three-dimensional tip position ($\hat{x}_t$, $\hat{y}_t$, $\hat{z}_t$), and its performance was quantitatively evaluated by computing the root mean square error (RMSE) with respect to the measured positions obtained from a motion-capture system.

For stable training, Min–Max scaling was applied to all inputs, and noise-reduction preprocessing was performed on the time-series sensor data. In addition, early stopping with a patience of 50 was introduced to prevent overfitting during training. Through these preprocessing and training strategies, a stable and high-accuracy learning model capable of reproducing the complex motion of a multi-DOF soft mechanism was successfully constructed.

3.2. Experimental setup

Fig. 11 illustrates the experimental system constructed for collecting the machine-learning dataset of the 3-DOF soft mechanism. In this system, each SAM is independently controlled from a PC through multiple electro-pneumatic (E/P) regulators, allowing individual assignment of arbitrary pressure inputs (P_{1t}, P_{2t}, P_{3t}). To monitor the actual pressure applied to each SAM, three pneumatic pressure gauges are installed independently. The three-channel outputs obtained from the optical fiber sensors embedded in each SAM are acquired via photodiode ICs and transferred to the PC. Additionally, a motion-capture system is

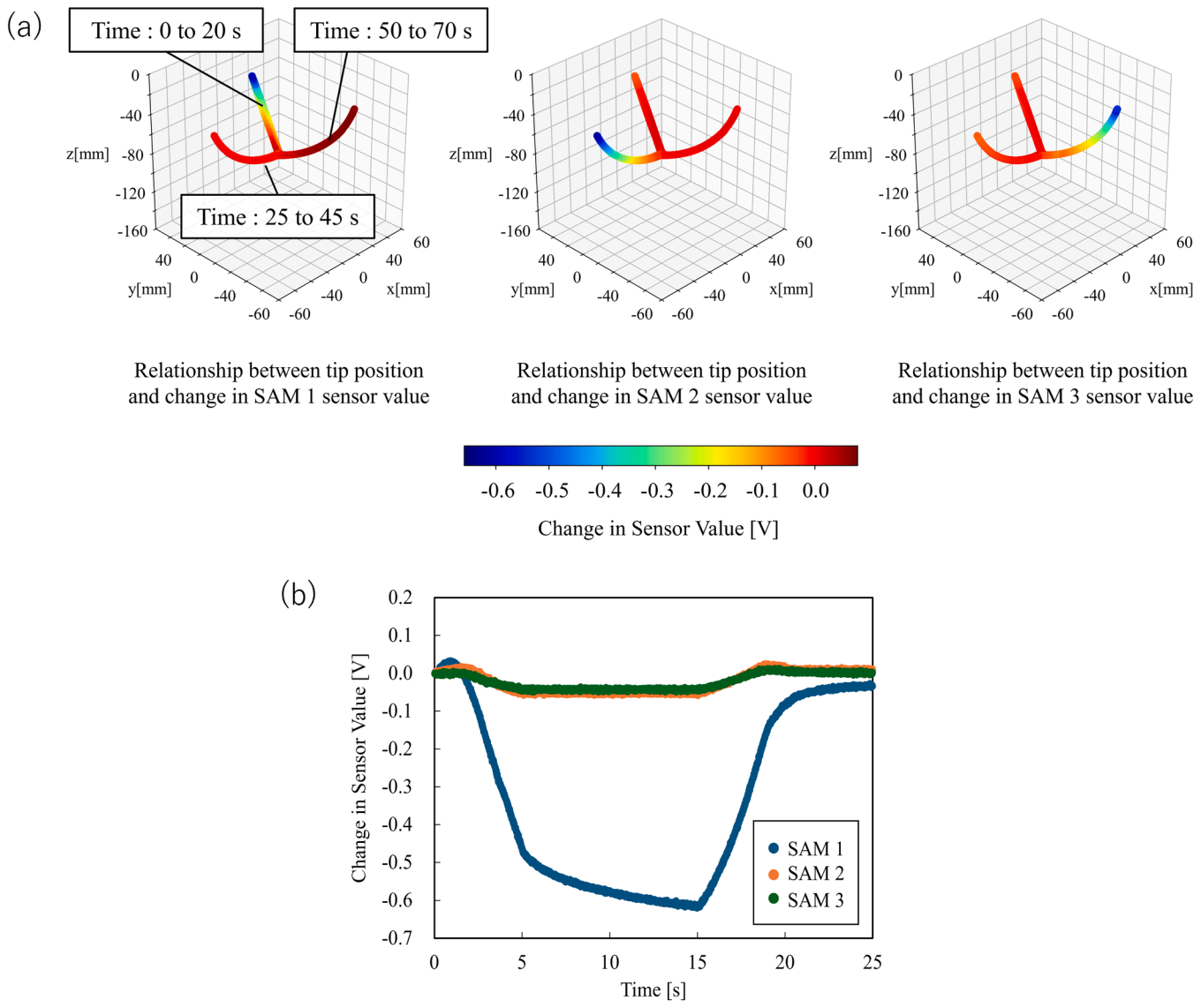

Fig. 9. Fundamental characteristics of the 3-DOF soft mechanism: (a) relationship between sensor outputs of SAM 1, SAM 2, and SAM 3 and the tip position, (b) time-series changes of sensor outputs of SAM 1, SAM 2, and SAM 3.

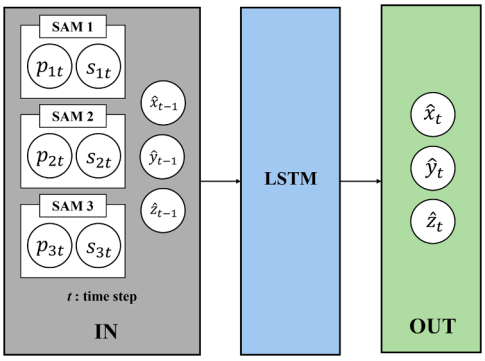

Fig. 10. LSTM-based neural network architecture for tip position estimation.

externally deployed to non-contact and accurately measure the tip motion of the mechanism.

All applied pressures, sensor outputs, and the measured tip position of the mechanism obtained from the motion-capture system are recorded on the PC as time-synchronized time-series data. These data constitute the dataset used to learn the complex multi-input–multi-output characteristics of the 3-DOF soft mechanism.

Table 1
Hyperparameters of the LSTM-based neural network model.

Parameter	Setting Value and Name
LSTM layers	3
LSTM layer neurons	200
Epochs	1000
Batch size	128
Data split rate	0.9
Look-back window	30
Learning rate	0.0001
Optimization algorithm	Adam
Loss function	Mean Squared Error

3.3. Results

Independently controlled pressures (P_{1t}, P_{2t}, P_{3t}) were randomly applied to the three SAMs (SAM 1, SAM 2, SAM 3) within the range of 0–300 kPa, with a sampling frequency of 100 Hz. During the experi-

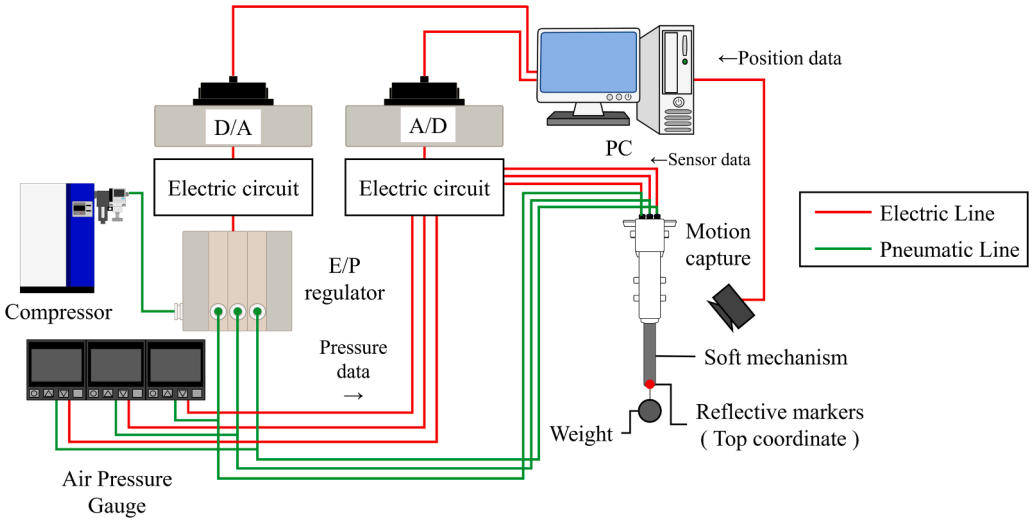

Fig. 11. Experimental system configuration for collecting machine-learning datasets.

Table 2
Tip position estimation error (MAE of Euclidean distance) for each model.

Model	MAE of Euclidean Distance [mm]
LSTM	0.25
MLR	17
MLP	6.9

Table 3
Tip position estimation error (MAE of Euclidean distance) of the LSTM model for different tip masses.

Tip Weight [g]	MAE of Euclidean Distance [mm]
0	0.25
100	0.33
200	0.27
300	0.26
400	0.19

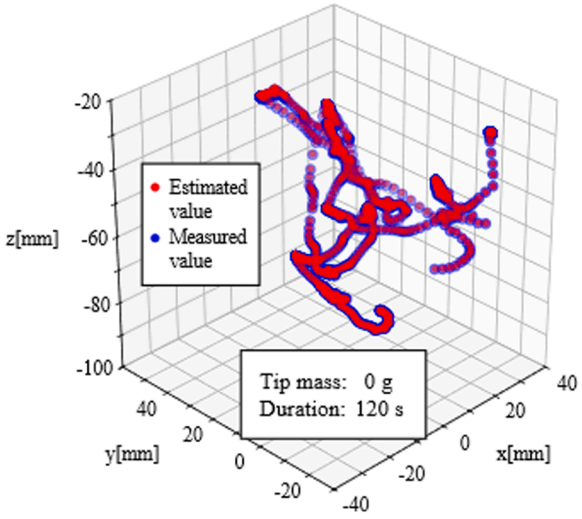

Fig. 12. Tracking performance of the tip position estimation using the LSTM model.

ments, the tip mass was fixed at one of five values (0, 100, 200, 300, or 400 g).

To assess generalization performance, the training dataset included only the 0 g, 200 g, and 400 g mass conditions, while the 100 g and 300 g conditions were excluded from training and used solely for evaluation.

The estimation accuracy was quantified using the Euclidean distance error between the LSTM model output and the ground-truth tip position measured by the motion-capture system. The Euclidean distance error e_t at time t is defined as

$$e_t = \sqrt{(x_t - \hat{x}_t)^2 + (y_t - \hat{y}_t)^2 + (z_t - \hat{z}_t)^2} \tag{2}$$

where $(x_t,\ y_t,\ z_t\ )$ denotes the ground truth and $(\hat{x}_t,\ \hat{y}_t,\ \hat{z}_t)$ denotes the predicted position. The mean absolute error (MAE), calculated as the average of e_t over all samples, was used as the primary evaluation metric, as it represents the average magnitude of the estimation error.

For comparison, two baseline models were implemented: a multivariate linear regression (MLR) model and a multilayer perceptron (MLP) model. For simplicity, the predicted variables are denoted as $(\hat{x}_t,\ \hat{y}_t,\ \hat{z}_t)$ for all models.

In the MLR model, the optical fiber sensor outputs $(S_{1t},\ S_{2t},\ S_{3t}\ \ )$ and the applied pressures $(P_{1t},\ P_{2t},\ P_{3t}\ \ )$ were used as explanatory variables, and the tip position of the mechanism was estimated through linear regression.

The relationship between the input vector $\boldsymbol{\beta}_t$ and the estimated tip position $\hat{\boldsymbol{\alpha}}_t$ is expressed as

$$\hat{\boldsymbol{\alpha}}_t = \mathbf{W}\boldsymbol{\beta}_t \tag{3}$$

where

$$\hat{\boldsymbol{\alpha}}_t = [\,\hat{x}_t\ \ \hat{y}_t\ \ \hat{z}_t\,]^{\mathrm{T}}, \qquad \boldsymbol{\beta}_t = [1\ \ S_{1t}\ \ S_{2t}\ \ S_{3t}\ \ P_{1t}\ \ P_{2t}\ \ P_{3t}]^{\mathrm{T}} \tag{4}$$

The regression coefficient matrix **W**is given by

$$\mathbf{w} = \begin{bmatrix} a_0 & a_1 & a_2 & a_3 & b_1 & b_2 & b_3 \\ c_0 & c_1 & c_2 & c_3 & d_1 & d_2 & d_3 \\ e_0 & e_1 & e_2 & e_3 & f_1 & f_2 & f_3 \end{bmatrix} \tag{5}$$

The same linear structure was applied independently to all three coordinates, forming a baseline model based on simple linear relationships between the SAM inputs and the tip position.

The MLP model consisted solely of fully connected layers and performed nonlinear mapping from inputs to outputs. Because the MLP does not incorporate temporal dependencies, its prediction at each time

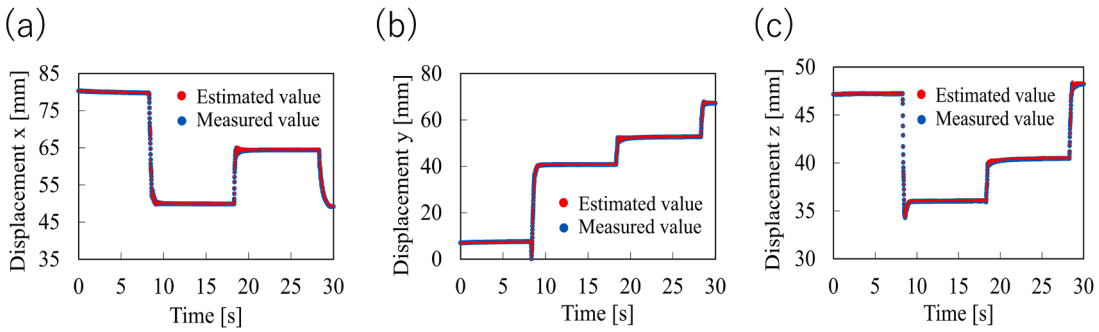

Fig. 13. Time-series tracking performance of the estimated and measured tip positions along each axis.

step relies only on information available at that time step. The inclusion of this model enables evaluation of the effect of explicitly modeling temporal dynamics in comparison with the LSTM approach.

Table 2 summarizes the tip-position MAE of the LSTM, MLP, and MLR models under the 0 g tip-mass condition. As shown, the LSTM model achieved the smallest error under all driving conditions, demonstrating the highest estimation performance. In contrast, the MLR model yielded the largest errors due to the inherent limitations of linear approximation in capturing highly nonlinear behaviors. The MLP model achieved moderate accuracy but lacked the ability to retain temporal information, resulting in larger errors than those of the LSTM. The LSTM is concluded to be a suitable model for estimating the three-dimensional tip position of the soft mechanism.

Table 3 summarizes the MAE of the LSTM model for tip masses of 0, 100, 200, 300, and 400 g. For the test datasets corresponding to the mass conditions used during training (0, 200, and 400 g), the MAE remained below 0.3 mm, indicating that the model achieved consistently high accuracy regardless of the applied load. Furthermore, for the unseen mass conditions of 100 g and 300 g, which were not included in the training dataset, the estimation errors also fell within a comparable range. These results demonstrate that the proposed model exhibits generalization capability.

Fig. 12 shows the three-dimensional trajectories of the estimated and ground truth over 120 s under the 0 g tip-mass condition. The estimated trajectory closely follows the ground truth.

The inference time of the LSTM model is approximately 5 ms, and the data acquisition sampling interval is 10 ms. Therefore, the overall end-to-end latency of the system is estimated to be approximately 15 ms. Fig. 13 shows the temporal response of the system. This figure corresponds to the experiment shown in Fig. 12 and presents the behavior along each axis from the start of estimation up to 30 s. The results confirm that the estimated values dynamically track the actual motion of the soft mechanism.

4. Conclusions

In this study, the 3-DOF soft mechanism using SAMs with the integrated optical fibers was developed and the LSTM model was applied for estimating the motion states of the mechanism. The experimental results showed that the LSTM model successfully learned the complex characteristics of the mechanism and achieved highly accurate tip position estimation.

The MAE, used as an index of estimation accuracy, was consistently smaller than those of the MLR and MLP models. In addition, the LSTM model indicated high generalization performance.

This work also confirmed the practicality of SAMs as actuators for constructing soft mechanisms. A notable advantage of SAMs is that sensing elements can be integrated directly into the actuators during fabrication, eliminating the need for additional external sensors when building the mechanism. This feature suggests that SAMs can function analogously to encoder-equipped motors in conventional mechatronic systems.

While previous studies have shown that LSTM-based estimation is effective for a single SAM, the present study verifies that LSTM remains effective even in a coupled multi-actuator soft mechanism. These findings indicate that LSTM-based modeling will be valuable for further development of soft mechanisms utilizing SAMs. Optical fiber-based sensing was achieved for the proposed mechanism by experimentally adjusting the LED input voltage in this study. Optical loss in the fiber is influenced by multiple factors, and a detailed analysis of its relationship with the applicable mechanism length remains as future work.

CRediT authorship contribution statement

Shun Miura: Investigation, Data curation. **Daisuke Yamaguchi:** Supervision. **Takefumi Kanda:** Supervision. **Rikimaru Okada:** Writing – original draft, Visualization, Validation, Methodology, Investigation, Formal analysis, Data curation. **Shuichi Wakimoto:** Writing – review & editing, Supervision, Project administration, Methodology, Investigation, Funding acquisition, Conceptualization. **Yuichiro Toda:** Software, Methodology, Formal analysis.

Declaration of Competing Interest

The authors declare that they have no known competing financial interests or personal relationships that could have appeared to influence the work reported in this paper.

Acknowledgements

This work was partially supported by JSPS KAKENHI (23K03644) and the Okayama Prefectural Special Power Source Science and Technology Promotion Project (FY 2025).

Data availability

Data will be made available on request.

References

[1] R.H. Gaylord, 1958, Fluid actuated motor system and stroking device, U.S. Patent 2,844,126, 1958.
[2] H.F. Schulte, The characteristics of the McKibben artificial muscle, in: The Application of External Power in Prosthetics and Orthotics, Natl. Acad. Sci., Washington, DC, 1961, pp. 94–115.
[3] C.P. Chou, B. Hannaford, Measurement and modeling of McKibben pneumatic artificial muscles, IEEE Trans. Robot 12 (1996) 90–102.
[4] G. Krishnan, J. Bishop-Moser, C. Kim, S. Kota, Kinematics of a generalized class of pneumatic artificial muscles, J. Mech. Robot 7 (4) (2015) 041014.
[5] J. Mei, S.L. Xie, H.T. Liu, J. Zang, Hysteresis modeling and compensation of pneumatic artificial muscles using the generalized Prandtl–Ishlinskii model, *Strojniški Vestnik*, J. Mech. Eng. 63 (2017) 657–665.
[6] B. Tondu, P. Lopez, Modeling and control of McKibben artificial muscle robot actuators, IEEE Control Syst. Mag. 20 (2) (2000) 15–38.
[7] M. Ide, T. Hashimoto, K. Matsumoto, H. Kobayashi, Evaluation of the power assist effect of muscle suit for lower back support, IEEE Access 9 (2021) 3249–3260.

[8] H. Zhang, J. Fan, Y. Qin, J. Han, M. Tian, Active neural network control for a wearable upper limb rehabilitation exoskeleton robot driven by pneumatic artificial muscles, IEEE Trans. Neural Syst. Rehabil. Eng. 32 (2024) 2589.
[9] K. Li, D. Zhang, Y. Chu, X. Zhao, S. Ren, X. Hou, A Pneumatic soft exoskeleton system based on segmented composite proprioceptive bending actuators for hand rehabilitation, Biomimetics 9 (2024) 638.
[10] R. Deimel, O. Brock, A novel type of compliant and underactuated robotic hand for dexterous grasping, Int. J. Robot. Res. 35 (2016) 161–185.
[11] Y. Zhang, H. Qi, Q. Cheng, Z. Li, L. Hao, Modeling and compensation of stiffness-dependent hysteresis coupling behavior for parallel pneumatic artificial muscle-driven soft manipulator, Appl. Sci. 14 (2024) 10240.
[12] J.D. Greer, T.K. Morimoto, A.M. Okamura, E.W. Hawkes, Series pneumatic artificial muscles (sPAMs) and application to a soft continuum robot, Proc. IEEE Int. Conf. Robot. Autom. (2017) 5503–5510.
[13] S. Wakimoto, K. Suzumori, T. Kanda, Development of intelligent McKibben actuator. Proc, IEEE/RSJ Int. Conf. Intelligent Robots and Systems, 2005, pp. 487–492.
[14] W. Felt, K.Y. Chin, C.D. Remy, Contraction sensing with smart braid McKibben muscles, IEEE/ASME Trans. Mechatron. 21 (2016) 1201–1209.
[15] M. Lalegani Dezaki, R. Sales, A. Zolfagharian, H. Yazdani Nezhad, M. Bodaghi, Soft pneumatic actuators with integrated resistive sensors enabled by multi-material 3D printing, Int. J. Adv. Manuf. Technol. 128 (2023) 4207–4221.
[16] A. Georgopoulou, L. Egloff, B. Vanderborght, F. Clemens, A soft pneumatic actuator with integrated deformation sensing elements produced exclusively with extrusion-based additive manufacturing, Eng. Proc. 6 (11) (2021).
[17] F. Furukawa, S. Wakimoto, T. Kanda, H. Hagihara, A soft master–slave robot mimicking octopus arm structure using thin artificial muscles and wire encoders, Actuators 8 (2) (2019) 40.
[18] K. Takaki, Y. Taguchi, S. Nishikawa, R. Niiyama, Y. Kawahara, Acoustic length sensor for soft extensible pneumatic actuators with a frequency characteristics model, IEEE Robot. Autom. Lett. 4 (4) (2019) 4292–4297.
[19] N. Saga, K. Shimada, D. Inamori, N. Saito, T. Satoh, J. Nagase, Smart pneumatic artificial muscle using a bend sensor like a human muscle spindle, Sensors 22 (2022) 8975.
[20] S. Kuriyama, M. Ding, Y. Kurita, T. Ogasawara, J. Ueda, Flexible sensor for McKibben pneumatic actuator, Proc. IEEE Sens. (2009) 520–525.
[21] R. Sakurai, M. Nishida, T. Jo, Y. Wakao, K. Nakajima, Durable pneumatic artificial muscles with electric conductivity for reliable physical reservoir computing, J. Robot. Mechatron. 34 (2022) 240–247.
[22] M.E. Giannaccini, C. Xiang, A. Atyabi, T. Theodoridis, S. Nefti-Meziani, S. Davis, Novel design of a soft lightweight pneumatic continuum robot arm with decoupled variable stiffness and positioning, Soft Robot 5 (2016) 54–70.
[23] R.L. Truby, C.Della Santina, D. Rus, Distributed proprioception of 3D configuration in soft, sensorized robots via deep learning, IEEE Robot. Autom. Lett. 5 (2) (2020) 3299–3306.
[24] T.G. Thuruthel, B. Shih, C. Laschi, M.T. Tolley, Soft robot perception using embedded soft sensors and recurrent neural networks, Sci. Robot 4 (2019) eaav1488.
[25] J. Shu, J. Wang, S.C.Y. Lau, Y. Su, K.H.L. Heung, X. Shi, Z. Li, R.K.Y. Tong, Soft robots' dynamic posture perception using kirigami-inspired flexible sensors and long short-term memory neural networks, Sensors 22 (2022) 7705.
[26] Y. Ni, S. Wakimoto, W. Tian, Y. Toda, T. Kanda, D. Yamaguchi, Length estimation of pneumatic artificial muscle with optical fiber sensor using machine learning, Sensors 25 (2025) 2221.
[27] W. Tian, S. Wakimoto, D. Yamaguchi, T. Kanda, Development of a smart artificial muscle using optical fibers, Smart Mater. Struct. 33 (2024) 055047.
[28] R.T. Schermer, J.H. Cole, Improved bend loss formula verified for optical fiber by simulation and experiment, IEEE J. Quantum Electron 43 (10) (2007) 899–909.
[29] X. Qu, F. Ma, S. Zhao, L. Yang, Z. Wu, B. Chen, Analysis of the influence of macro-bending loss in single-mode optical fibers on OFDR signal quality, Sensors 25 (2025) 6983.
[30] A. Ashfaq, Y. Chen, K. Yao, G. Sun, J. Yu, Microbending loss caused by stress in optical fiber composite low-voltage cable, Proc. IEEE Int. Conf. Prop. Appl. Dielectr. Mater. (2018) 483–486.
[31] S. Hochreiter, J. Schmidhuber, Long short-term memory, Neural Comput. 9 (1997) 1735–1780.
[32] N. Srivastava, G. Hinton, A. Krizhevsky, I. Sutskever, R. Salakhutdinov, Dropout: a simple way to prevent neural networks from overfitting, J. Mach. Learn. Res. 15 (2014) 1929–1958.
[33] T. Lin, B.G. Horne, P. Tino, C.L. Giles, Learning long-term dependencies in NARX recurrent neural networks, Trans. Neural Netw. 7 (1996) 1329–1338.

Rikimaru Okada received his M.Eng. degree from Okayama University, Japan, in 2026.

Shuichi Wakimoto received his Ph.D. degree from Okayama University, Japan, in 2007. He was a Research Fellow of the Japan Society for the Promotion of Science from 2004 to 2007. From 2007–2011, he was an Assistant Professor at Okayama University, Japan. From 2012–2025, he was an Associate Professor at the same university. He is currently a Professor at Okayama University, Japan.

Yuichiro Toda received his Ph.D. degree from Tokyo Metropolitan University, Japan, in 2017. He was a Research Fellow of the Japan Society for the Promotion of Science from 2013 to 2016. From 2017–2018, he was a Project Assistant Professor at Tokyo Metropolitan University, Japan. From 2018–2022, he was an Assistant Professor at Okayama University, Japan. He is currently an Associate Professor at the same university.

Shun Miura received his B.Eng. degree from Okayama University, Japan, in 2026.

Daisuke Yamaguchi received his Ph.D. degree from Okayama University, Japan, in 2014. He was a Research Fellow of the Japan Society for the Promotion of Science from 2013 to 2014. From 2014–2020, he was an Assistant Professor at Saitama University, Japan. He is currently an Assistant Professor at Okayama University, Japan.

Takefumi Kanda received his Ph.D. degree from the University of Tokyo, Japan, in 2002. He was a Research Associate and Lecturer at Okayama University, Japan. From 2007–2017, he was an Associate Professor at Okayama University. He is currently a Professor at the same university.